Online Research @ Cardiff

This is an Open Access document downloaded from ORCA, Cardiff University's institutional repository: https://orca.cardiff.ac.uk/id/eprint/125826/

This is the author's version of a work that was submitted to / accepted for publication.

Citation for final published version:

Pudkon, Watcharapong, Kaowphong, Sulawan, Pattisson, Samuel, Miedziak, Peter J., Bahruji, Hasliza, Davies, Thomas E., Morgan, David J. ORCID: https://orcid.org/0000-0002-6571-5731 and Hutchings, Graham J. ORCID: https://orcid.org/0000-0001-8885-1560 2019. Microwave synthesis of ZnIn2S4/WS2 composites for photocatalytic hydrogen production and hexavalent chromium reduction. Catalysis Science and Technology 9 (20) , pp. 5698-5711. 10.1039/C9CY01553A filefile

Publishers page: http://dx.doi.org/10.1039/C9CY01553A <http://dx.doi.org/10.1039/C9CY01553A>

Please note:
Changes made as a result of publishing processes such as copy-editing, formatting and page numbers may not be reflected in this version. For the definitive version of this publication, please refer to the published source. You are advised to consult the publisher's version if you wish to cite this paper.

This version is being made available in accordance with publisher policies. See http://orca.cf.ac.uk/policies.html for usage policies. Copyright and moral rights for publications made available in ORCA are retained by the copyright holders.

information services
gwasanaethau gwybodaeth

Microwave synthesis of $ZnIn_2S_4/WS_2$ composites for photocatalytic hydrogen production and hexavalent chromium reduction

Watcharapong Pudkon[a,b], Sulawan Kaowphong[a,c], Samuel Pattisson[d], Peter J. Miedziak[d,e], Hasliza Bahruji[d], Thomas E. Davies[d], David J. Morgan[d] and Graham J. Hutchings[d]

[a]*Department of Chemistry, Faculty of Science, Chiang Mai University, Chiang Mai 50200, Thailand*

[b]*Graduate School, Chiang Mai University, Chiang Mai 50200, Thailand*

[c]*Center of Excellence in Materials Science and Technology, Chiang Mai University, Chiang Mai 50200, Thailand*

[d]*Cardiff Catalysis Institute, School of Chemistry, Cardiff University, Main Building, Park Place CF10 3AT, Cardiff, UK*

[e]*School of Applied Sciences, University of South Wales, Pontypridd CF37 4AT, UK*

Abstract

A rapid microwave synthesis route for the fabrication of $ZnIn_2S_4$ powder and $ZnIn_2S_4/WS_2$ composite is presented. Firstly, effect of different sulfur sources – thioacetamide and L-cysteine – on the physicochemical properties and photocatalytic H_2 production of the synthesized $ZnIn_2S_4$ were investigated. It was found that well-defined flower-like $ZnIn_2S_4$ microspheres obtained from L-cysteine facilitated a relatively higher H_2 production rate. Then, different loadings of WS_2 were introduced into the well-defined flower-like $ZnIn_2S_4$ microspheres aiming to improve its photocatalytic H_2 production. Compared to the pure $ZnIn_2S_4$ and WS_2, all $ZnIn_2S_4/WS_2$ composite photocatalysts exhibited enhanced photocatalytic H_2 production in the presence of Na_2S/Na_2SO_3 as sacrificial reagents under UV-visible irradiation, where the $ZnIn_2S_4/WS_2$-40%wt composite had the highest photocatalytic activity. For this material, 293.3 and 76.6 μmol h^{-1} g^{-1} of H_2 gas were produced under UV-visible and visible light irradiation respectively. In addition, the photoreduction activity of hexavalent chromium (Cr(VI)) by the $ZnIn_2S_4/WS_2$-40%wt was also investigated under visible light irradiation and it was observed that 98.5% of Cr(VI) was reduced within 90 min at pH 4.

Keywords: $ZnIn_2S_4/WS_2$, Microwave synthesis, Heterostructure, H_2 production, Cr(VI) reduction

1. Introduction

Photocatalysis has attracted considerable as a sustainable approach for solving environmental and energy problems that face society as a whole. Production of hydrogen from photocatalytic water splitting is regarded as the promising strategies for conversion of solar energy to chemical energy.[1] [2] [3] In addition, the elimination of heavy metal ions from wastewater is also considered to be an important research target for photocatalysis.[4] Growth of new technologies based on photocatalysts for water splitting and hexavalent chromium (Cr(VI)) reduction using semiconductors has evolved from the initial utilization of metal oxide semiconductors, to second-generation semiconductor involving doped metal oxides as well as two-dimensional (2-D) semiconductors.[5] Semiconductors such as TiO_2, ZnO and CdS are able to utilize photons under ultraviolet radiation which makes up 4% of the solar incident light. Doping TiO_2 with a third element such as C, S or metal doping can improve the solar light utilization in the visible light region.[6] The investigation of ultrathin 2-D semiconductors with superior activity for enhancing photon absorption and electron-hole utilization has recently attracted significant interest as a new generation of photocatalysts.[7] Layered-structure semiconductors with nanolayer thickness, in principle, possess a high surface area for photon absorption, substrate adsorption and generation of highly active oxidizing species.[8] Nevertheless, this principle is based on the ability of the semiconductor to take full advantage of the photons in the entire solar spectrum, to efficiently separate the photo-generated charge carriers and finally remain robust and stable to drive the water oxidation/reduction reaction. Improved visible-light-driven photocatalysts are now required to promote the efficiency of solar energy conversion.

$ZnIn_2S_4$, the only member of the AB_2X_4 family of semiconductors with a single-layered structure, has attracted interest because of its potential applications in the fields of charge storage, thermoelectricity, hydrogen production and as photodetectors.[9] [10] [11] [12] $ZnIn_2S_4$ is an

ideal candidate as an active photocatalyst to drive photocatalytic water splitting[13] and photocatalytic Cr(VI) reduction[14] in the visible light region due to its photochemical stability and narrow band gap energy (2.75 eV). In addition, the layered structure of $ZnIn_2S_4$ can increase the exposure of the interlayer sulfur atom which increases the interaction with oxygen as the active photo-generated carrier scavenger.[15] However, its photocatalytic efficiency is still under scrutiny with concern about its narrow band gap that can contribute to fast recombination of photo-generated charge carriers. The charge carrier recombination is classified into two types: bulk recombination and surface recombination.[16] Decreasing the bulk recombination can be achieved by fabricating the $ZnIn_2S_4$ 2-D microstructure which in principle can shorten the distance for the charge carrier to travel to its surface and also can reduce the impurities and defects in the $ZnIn_2S_4$ crystal.[17] Modification of the $ZnIn_2S_4$ by introducing surface defects, constructing heterojunction structure, and co-doping with metals can prevent surface recombination.[18 19 20] Doping transition metals or noble metals on the surface of $ZnIn_2S_4$ can improve the photocatalytic efficiency of the $ZnIn_2S_4$ but the light absorption efficiency is limited particularly at high metal loadings.[21 22] In addition, noble metals are expensive and this can limit their wider application as components of photocatalysts.[18 23] Combination of $ZnIn_2S_4$ with another semiconductor is therefore a feasible alternative to suppress the recombination of the photo-generated charge carriers. For example, $ZnIn_2S_4$/CdS, $ZnIn_2S_4$/In_2S_3, $ZnIn_2S_4$/$K_2La_2Ti_3O_{10}$, $ZnIn_2S_4$/$CdIn_2S_4$ have all shown efficacy.[24 25 26 27] The previous studies have shown that transition metal dichalcogenides (TMDs) such as MoS_2, $MoSe_2$ and WS_2 are efficient co-catalysts for improving photocatalytic H_2 production and heavy metal pollutants removal.[28 29 30 31 32] Among these TMDs, WS_2 is an effective candidate for solar energy conversion due to its narrow band gap energy, a less electronegative valence band, a high reducing activity of conductive band, and a strong W-S bond.[33] In addition, it is an important material for a wide range of applications including catalysis, batteries and optical devices.[33 34]

[35] As well as an active component in many hydrogenation reactions such as hydro-denitrogenation and hydro-desulfurization.[36 37]

As the conduction band (C_B) of WS_2 is less negative than that of $ZnIn_2S_4$, a directional electron transfer from the C_B of $ZnIn_2S_4$ to the C_B of WS_2 and a migration of the photo-generated holes in the valence band (V_B) in the opposite way can be enabled.[38 39 40] Therefore, WS_2 is a potential co-catalyst for enhancing the photocatalytic activity of $ZnIn_2S_4$ since the charge separation would be promoted and the charge recombination would be suppressed. Herein, we reported the microwave synthesis of flower-like $ZnIn_2S_4$ microspheres and $ZnIn_2S_4/WS_2$ composite for photocatalytic applications. This method was chosen in this work because the interaction between a microwave radiation and polar molecules in a reaction system offers a homogeneous heating with fast reaction rate as compared to the conventional heating methods. Therefore, the desired materials with high purity, high crystallinity, and uniform shape and size can be produced with a short time period and reduced processing temperature, leading to a relatively low energy demand for materials production.[41] In this work, well-defined flower-like $ZnIn_2S_4$ microspheres were first synthesized using an appropriate sulfur source for H_2 production from photocatalytic water splitting under UV-visible light irradiation. Then, the $ZnIn_2S_4/WS_2$ composites with different loading amounts of WS_2 were fabricated in an attempt to enhance the H_2 production rate. In addition, recyclability of the $ZnIn_2S_4/WS_2$ photocatalyst was also assessed for its practical use. Furthermore, potential use of the $ZnIn_2S_4/WS_2$ photocatalyst for Cr(VI) photoreduction – a model of heavy metal ions – was also investigated. Possible photocatalytic mechanisms for enhanced photocatalytic activities of the $ZnIn_2S_4/WS_2$ heterojunction were also proposed.

2. Materials and methods

2.1. Preparation of photocatalysts

All the chemicals were analytical grade and used without further purification as they were received. In a typical synthesis, $ZnCl_2$ (2.0 mmol), $InCl_3 \cdot 4H_2O$ (4.0 mmol) and a sulfur source (L-cysteine or thioacetamide, 10.0 mmol) were dissolved in de-ionized water (20.0 mL). After constant stirring for 20 min, the solution was transferred into a dissolution vessel with a capacity of 50.0 mL. The vessel was sealed and exposed to microwave radiation in a microwave oven operated at 100 W for 1 h and then naturally cooled to room temperature. Finally, the dark green yellow powder was separated from the mother liquor by a vacuum filtration, then washed with de-ionized water several times and dried (80 °C, 24 h).

To synthesize $ZnIn_2S_4/WS_2$ composites, the synthesized $ZnIn_2S_4$ and commercial WS_2 were dispersed in de-ionized water (20 mL) with vigorous stirring. The solution was then transferred into a dissolution vessel with a capacity of 50.0 mL. The vessel was sealed and exposed to microwave radiation in a microwave oven operated at 100 W for 1 h and then naturally cooled to room temperature. Finally, a dark-green powder was separated from the mother liquor by centrifuged and dried (80 °C, 24 h). The composites with different loading amounts of WS_2 were denoted as ZIS/WS-x%, where the x represents 20, 30, 40, 50, 60 and 80%wt of WS_2. In addition, the $ZnIn_2S_4/WS_2$-40%wt composite was also prepared by a physical grinding without the microwave treatment for comparison.

2.2. Characterization

X-ray diffraction (XRD) patterns were recorded by a Rigaku Miniflex II X-ray diffractometer, using a CuK_α radiation source (40 kV and 40 mA) and Ni attenuator. UV-visible diffuse reflectance spectra (UV-visible DRS) of the samples were obtained using an Agilent Technologies, Cary Series UV-visible spectrophotometer. The wavelength scans were

collected in the range of 200-800 nm, at a scan rate of 150 nm/min. Brunauer-Emmett-Teller (BET) surface areas were determined by N_2 adsorption at -196 °C using a Quantachrome Quadrasorb-*evo* instrument. The samples were prepared by removing physically adsorbed water at 120 °C for 3 h under vacuum. Scanning electron microscopy (SEM) images were obtained on TESCAN MAIA3 equipped with an Oxford Instruments X-Max^N 80 energy dispersive X-ray (EDX) detector. The samples were mounted on a Carbon Lite adhesive disk attached to an aluminium stub. X-ray photoelectron spectroscopy (XPS) was analyzed using a Kratos Axis Ultra DLD system with a monochromatic Al K_α X-ray source operating at 120 W and analyzer pass energies of 160 eV. The XPS data were analyzed using Casa XPS software. Photoluminescence (PL) spectra were examined by an Avantes AvaSpec-2048TEC-USB2 photoluminescence spectrometer with an excitation wavelength of 590 nm.

Electrochemical impedance spectroscopy (EIS) and Mott-Schottky analysis were performed using a three-electrode electrochemical system. A working electrode was fabricated as follows, a certain amount of the photocatalyst (0.10 g) was dispersed in a mixture of isopropanol and de-ionized water (40:20 %v/v) by ultrasonic treatment. The dispersion was dropped on a fluorine-doped tin oxide (FTO) coated glass with a fixed area of 1x1 cm^2. After evaporation, the photocatalyst was attached to the FTO glass surface. For counter and reference electrodes, a platinum (Pt) plate and Ag/AgCl were used, respectively. Na_2SO_4 aqueous solution (0.1 M) was used as an electrolyte solution. The Autolab Potentiostat/galvanostat (PGSTAT128N, Metrohm Siam Ltd.) was used for all the tests. The EIS spectra, measured at a frequency range of alternating current was 0.1 Hz - 100 kHz at 1.5 V, were fitted to an appropriate electric analog by the Nova 2.1.3 software. The Mott–Schottky plots were measured at a frequency of 100 Hz. The following equation was used to convert the measured potential *vs*. Ag/AgCl to the NHE; $E_{NHE} = E_{Ag/AgCl} + E^o_{Ag/AgCl}$, where $E^o_{Ag/AgCl}$ (3.0 M KCl) = 0.21 V at 25 °C.

2.3. Photocatalytic reactions

The H_2 production experiment was carried out in a Pyrex flask (150 mL) fitted with a purge line and a septum for sampling. Reactions were carried out with a suspension of photocatalyst (0.10 g) in a sacrificial reagent which consisted of 0.35 M Na_2S mixed 0.25 M Na_2SO_3 solution (40 mL) and de-ionized water (60 mL). Before the reaction, the mixture was purged with argon gas for 30 min to remove dissolved air. The mixture was illuminated with a 150 W Xe arc lamp (Oriel Model 66084, light source 10 cm from the vessel) under constant stirred. Gas samples (0.5 mL) were taken periodically and analyzed for H_2 using a gas chromatograph (PerkinElmer Clarus 480). The apparent quantum yields (AQY) of the pure $ZnIn_2S_4$ and composite photocatalysts for the H_2 production were calculated according to the following equation [42]:

$$\mathrm{AQY}(\%) = \frac{2 \times \text{number of evolved } H_2 \text{ molecules}}{\text{number of incident photon}} \times 100$$

where the light intensity is 119.43 mW/cm^2 and the light spot area is 12.56 cm^2 with a 400 nm band pass filter. The "2" value means that two electrons are necessary for the formation of one hydrogen molecule, and, correspondingly, it is required that two photons interact with the photocatalyst.

The photoreduction of Cr(VI) was performed under a suspension of the photocatalyst (0.10 g) in a $K_2Cr_2O_7$ solution (10 ppm, 200 mL) and the pH of reaction suspension was adjusted by adding 1 M HCl or 1 M NH_4OH. The suspension was placed in the dark and stirred for 30 min to achieve the adsorption-desorption equilibrium. After that, the mixture was irradiated under a 50 W LED white light with a fixed distance from the light source to the reactor at 8.5 cm. During the photocatalytic reaction, the suspension (5 mL) was sampled every 30 min. Then, 1,5-diphenylcarbazide and H_2SO_4 were added into the sampling to form a Cr(VI)-diphenylcarbazide complex, which gives a reddish-purple color. Finally, the complex

solution was measured at its maximum absorption wavelength of 532 nm by using a UV-visible spectrophotometer (UV-1800 Shimadzu). The photoreduction efficiency was calculated using the following equation: %Photoreduction efficiency = $[(C_0\text{-}C)/C_0]$ x 100, where C_0 and C are the concentrations of the Cr(VI) complex when adsorption-desorption equilibrium is achieved and after light irradiation, respectively. A blank experiment (without any photocatalyst) was also carried out under the same conditions. The apparent quantum yields (AQY) of the pure $ZnIn_2S_4$ and composite photocatalysts for the Cr(VI) reduction were calculated according to the following equation [43] :

$$\text{AQY}(\%) = \frac{3 \text{ x number of reduced Cr(VI) ions}}{\text{number of incident photon}} \times 100$$

where the light intensity is 54.95 mW/cm^2 and the light spot area is 6.25 cm^2 with a 400 nm band pass filter. The "3" value means that three electrons are necessary for the formation of one Cr(III) ion, and, correspondingly, it is required that three photons interact with the photocatalyst.

3. Results and discussion

3.1. Influence of the sulfur source on the physicochemical properties and photocatalytic activity of $ZnIn_2S_4$

The XRD patterns of the synthesized powders obtained from the two different sulfur sources (Fig. 1a) provide an information on their crystal structure and crystallinity. The main diffraction reflections are observed at 2θ of 21.2°, 27.9°, 30.1°, 39.9°, 47.3°, 51.8° and 55.5°, respectively representing the (006), (102), (104), (108), (110), (116) and (202) crystal planes of hexagonal $ZnIn_2S_4$ (JCPDS database no. 01-072-0773). $ZnIn_2S_4$ synthesized using the microwave synthesis method are well-crystallized with no characteristic reflections of possible impurities such as ZnS, In_2S_3 or the corresponding metal oxides. The crystallite size of the

$ZnIn_2S_4$ particles was calculated from the (110) reflection by applying the Debye-Scherrer equation.[44] The calculated crystallite size of the $ZnIn_2S_4$ synthesized using L-cysteine is smaller than that using thioacetamide as presented in Table 1.

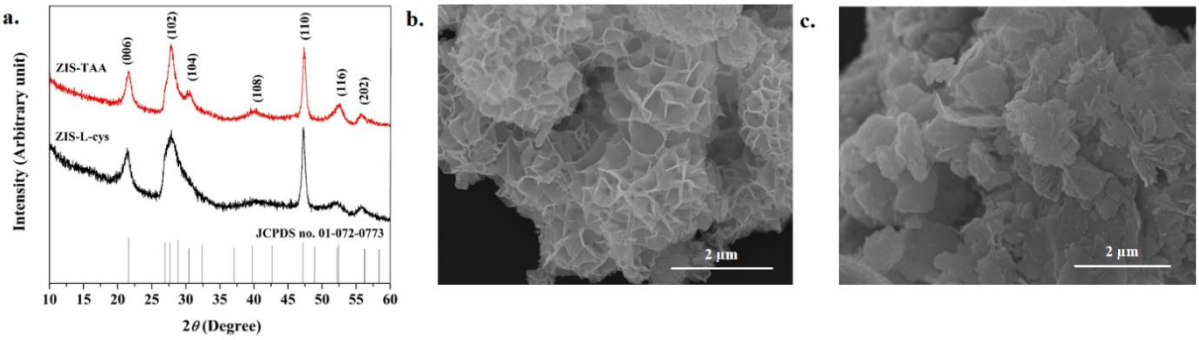

Fig. 1. a.) XRD patterns, and SEM images of the $ZnIn_2S_4$ powders synthesized using **b.)** L-cysteine (ZIS-L-cys) and **c.)** thioacetamide (ZIS-TAA) as sulfur sources.

Table 1 Comparison of calculated crystallite size, surface area, absorption edge and band gap energy of the $ZnIn_2S_4$ synthesized using different sulfur sources.

Sulfur sources	**Crystallite size (nm)**	**Surface area (m^2/g)**	**Absorption edge (nm)**	**Band gap energy (eV)**
L-cysteine	12.58	46	440	2.81
thioacetamide	14.38	28	500	2.48

SEM images of $ZnIn_2S_4$ synthesized using L-cysteine and thioacetamide are presented in Fig. 1b and 1c, respectively. $ZnIn_2S_4$ synthesized using L-cysteine has well-defined flower-like microspheres ranging from 3 to 6 µm in diameter. Such microspheres comprise interconnecting nanosheets, resulting in a porous structure on the surface of the $ZnIn_2S_4$ microspheres. Using thioacetamide as the sulfur source, the $ZnIn_2S_4$ particles exhibit accumulated curled nanosheets on their surface can be observed. The BET surface area analysis of the $ZnIn_2S_4$ particles (summarized in Table 1) indicates that the $ZnIn_2S_4$ particles synthesized using L-cysteine show

relatively higher surface area (46 m^2/g) than those synthesized using thioacetamide (28 m^2/g). In addition, elemental analysis reveals that the mole ratio of Zn:In:S is 1: 2.3: 4.08, in a good agreement with the stoichiometry of $ZnIn_2S_4$.

The formation of the hexagonal $ZnIn_2S_4$ flower-like microspheres, reported by Chen et al.[45] , occurs *via* two main steps: (i) the formation of hexagonal $ZnIn_2S_4$ nuclei through the reaction among the starting reagents and (ii) the intrinsic anisotropic growth of the produced $ZnIn_2S_4$ nuclei into an hexagonal lamellar structure. Subsequently, the flower-like microspheres are formed from the self-assembly of the nanosheets. In this research, the difference in the microstructure of the $ZnIn_2S_4$ microspheres is possibly related to the molecular structures of L-cysteine and thioacetamide, and the rate of S^{2-} ions released during the microwave heating process. Although both L-cysteine and thioacetamide can coordinate with inorganic cations to form metal-ligand complexes, the functional groups of L-cysteine molecule (-NH_2, -COOH and -SH) have a stronger affinity to coordinate with the metal ions comparing with the functional groups of thioacetamide (-NH_2 and -SH).[46 47] Consequently, the rate of S^{2-} ions released from the metal-L-cysteine complex is slower than that from the metal-thioacetamide complex.[48] As a result, the hexagonal $ZnIn_2S_4$ nuclei are slowly produced and consequently well-crystallized $ZnIn_2S_4$ nanosheets are gradually formed. Finally, accelerated by microwave heating, the adjacent nanosheets are self-assembled to form flower-like $ZnIn_2S_4$ microspheres. In addition, the steric hindrance of L-cysteine molecules can prevent the accumulation of nanoplate-clusters on the surface of the $ZnIn_2S_4$ microspheres, enabling the construction of open pore structure on the $ZnIn_2S_4$ microspheres surface.

The surface electronic states and chemical composition of the $ZnIn_2S_4$ microspheres synthesized using L-cysteine were investigated by XPS analysis and are shown in Fig. 2a. The high-resolution spectrum of Zn 2p shows the binding energy at 1022.03 eV and 1045.08 eV, which are ascribed to Zn $2p_{3/2}$ and Zn $2p_{1/2}$ respectively. The In 3d spectrum of shows two peaks

centered at the binding energy of 445.08 eV (In $3d_{5/2}$) and 452.63 eV (In $3d_{3/2}$). The spectrum of S 2p indicates that the signal can be convoluted into two peaks. One is located at 161.88 eV (S $2p_{3/2}$) and the other at 162.88 eV (S $2p_{1/2}$). These binding energy values correspond to the chemical valence sates of Zn^{2+}, In^{3+} and S^{2-}, respectively.[49] The UV-visible DRS spectra of $ZnIn_2S_4$ (Fig. 2b) show an absorption edge in the visible region (located around 450-500 nm). Band gap energy (Table 1), calculated from the absorption edges, of the $ZnIn_2S_4$ synthesized using L-cysteine (2.81 eV) is larger than that synthesized using thioacetamide (2.48 eV).

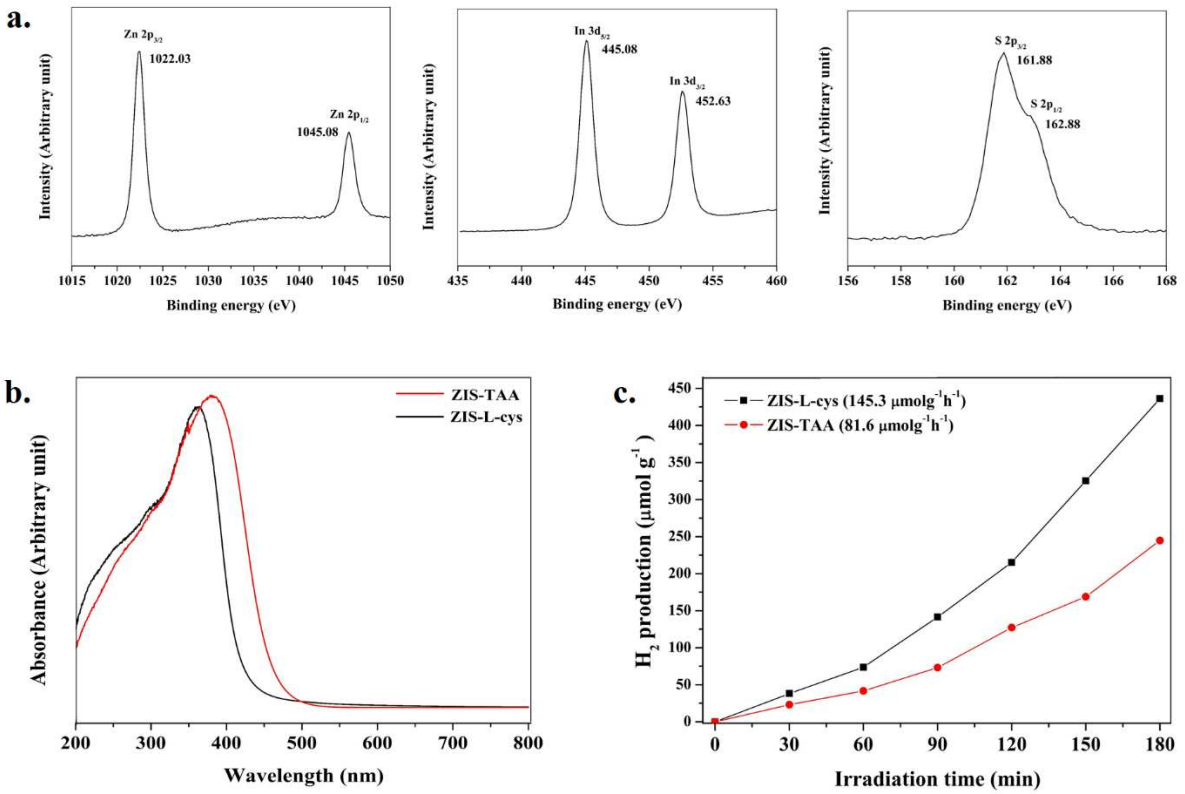

Fig. 2. a.) High resolution XPS spectra of Zn 2p, In 3d and S 2p for the $ZnIn_2S_4$ powders synthesized using L-cysteine; **b.)** UV-visible DRS spectra of the $ZnIn_2S_4$ synthesized using different sulfur sources and **c.)** H_2 production rate during 3 h reaction on the $ZnIn_2S_4$ photocatalyst synthesized using different sulfur sources under Xenon light irradiation.

The photocatalytic activity for H_2 production of the $ZnIn_2S_4$ photocatalyst was evaluated using 0.35 M Na_2S and 0.25 M Na_2SO_3 mixed aqueous solution under UV-visible irradiation

for 3 h. As shown in Fig. 2c, the H_2 production rate of the $ZnIn_2S_4$ photocatalyst synthesized using L-cysteine (145.3 µmol h^{-1} g^{-1}) is higher than that synthesized using thioacetamide (81.6 µmol h^{-1} g^{-1}). This we consider is related to the well-defined flower-like $ZnIn_2S_4$ microspheres with the open pore structure can permit multi-reflection of an incident light in its structure which facilitates a longer life-time of the incident light, thereby more electron-hole pairs can be generated.[50] Moreover, the higher surface area of the $ZnIn_2S_4$ photocatalyst can offer more active sites exposed to the reactants during the photocatalytic processes, as a result, the photocatalytic reaction can occur more easily.[51] In addition, the wider band gap energy of the well-defined flower-like $ZnIn_2S_4$ microspheres would reduce the recombination process of the photo-generated electrons and holes which is available for the photocatalytic reactions.[52] As discussed above, the $ZnIn_2S_4$ synthesized using L-cysteine was chosen to combine with WS_2 in order to improve photocatalytic activity in the production of H_2.

3.2. Influence of the loading amount of WS_2 on the physicochemical properties of $ZnIn_2S_4/WS_2$ composite

The $ZnIn_2S_4/WS_2$ composites with different loading amounts of WS_2 were prepared by the microwave synthesis method. The XRD patterns (Fig. 3a) of the $ZnIn_2S_4/WS_2$ composite samples with 20, 40, 60, and 80%wt of WS_2, show the main diffraction reflections of a hexagonal $ZnIn_2S_4$ structure (JCPDS database no.01-072-0773) with the additional reflections at 14.3°, 33.7°, 39.5° and 58.4° which correspond to a hexagonal WS_2 structure (JCPDS no.00-008-0237). This result implies that the introduction of WS_2 through microwave heating treatment does not affect the hexagonal $ZnIn_2S_4$ crystal structure. In addition, the diffraction reflection intensity of WS_2 is gradually increase with increasing amounts of WS_2 in the composites, while the diffraction reflection intensity of $ZnIn_2S_4$ is gradually decrease. The UV-visible DRS spectra of $ZnIn_2S_4$, WS_2, and $ZnIn_2S_4/WS_2$-40%wt are shown in Fig. 3b.

Compared to $ZnIn_2S_4$, the absorption edge of the $ZnIn_2S_4/WS_2$-40%wt composite shifts to a higher wavelength due to the presence of WS_2. This suggests that the $ZnIn_2S_4/WS_2$ composite has improved visible light response after introducing WS_2, thereby promoting a generation of electron-hole pairs. Therefore, the enhanced photocatalytic activity is expected from the $ZnIn_2S_4/WS_2$ heterostructure under visible light irradiation.

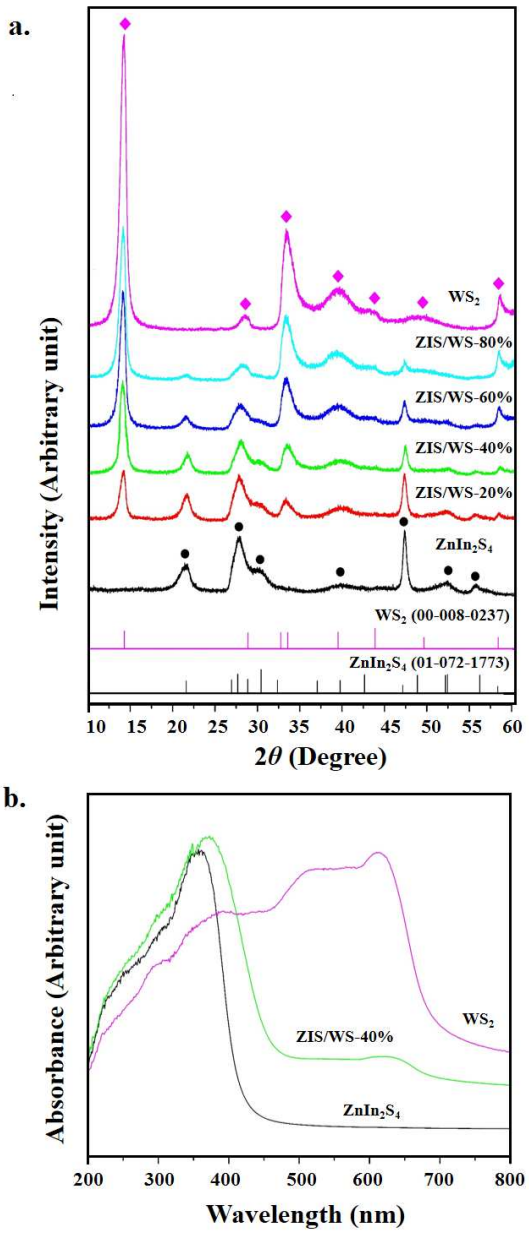

Fig. 3. a.) XRD patterns and **b.)** UV-visible DRS spectra of the synthesized powders.

Fig. 4 shows the XPS spectrum of the $ZnIn_2S_4/WS_2$-40%wt composite compared with $ZnIn_2S_4$ and WS_2. In Fig. 4(a-c), the XPS spectra of the $ZnIn_2S_4/WS_2$-40%wt composite show binding energy of Zn 2p, In 3d and S 2p, corresponding to $ZnIn_2S_4$. The XPS spectra of W 4f are shown in Fig. 4d. The binding energy at 32.58, 34.78and 38.28 eV correspond to W $4f_{7/2}$, W $4f_{5/2}$ and W 4f $_{3/2}$, respectively.[34] These results confirm the coexistence of $ZnIn_2S_4$ and WS_2 in the composite. In addition, the binding energies of Zn 2p, In 3d and S 2s are shifted to higher values after introducing WS_2. While, the binding energies of W 4f are slightly shifted to lower values in comparison to pure WS_2. These indicate that the chemical environments of Zn^{2+}, In^{3+}, W^{4+} and S^{2-} ions in the $ZnIn_2S_4$ and WS_2 structures are changed, showing a chemical interaction at the contact interface of the $ZnIn_2S_4/WS_2$ heterostructure rather than a physical contact between the two separate $ZnIn_2S_4$ and WS_2 materials.

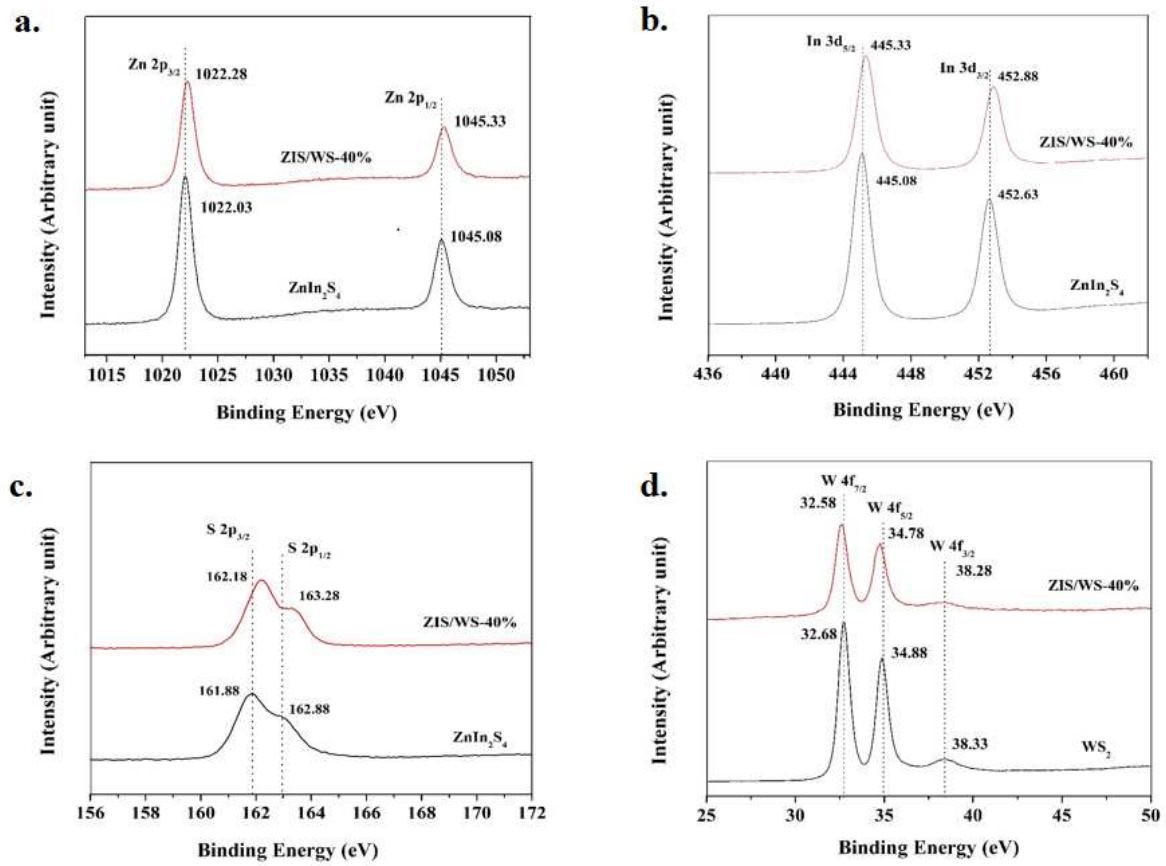

Fig. 4. High resolution XPS spectra of **a.)** Zn 2p, **b.)** In 3d, **c.)** S 2p and **d.)** W 4f of the $ZnIn_2S_4/WS_2$-40%wt composite compared with $ZnIn_2S_4$ and WS_2.

SEM images of the $ZnIn_2S_4$, WS_2, and $ZnIn_2S_4/WS_2$-40%wt powders are presented in Fig. 5a-5c. The SEM image of the $ZnIn_2S_4/WS_2$-40%wt composite (Fig. 5c) reveals that the nanoparticles with the average diameter of about 80 nm of the WS_2 (Fig. 5b) are dispersed on the surface of the flower-like $ZnIn_2S_4$ microspheres (Fig. 5a). The TEM images (Fig. 5d) indicate that the WS_2 nanoparticles are closely attached to the flower-like $ZnIn_2S_4$ microsphere in which the microsphere are developed by stacking of multiple nanosheet layers with 1.68 nm thickness. The HRTEM image of the WS_2 nanoparticle in the composite reveals the 0.62 nm lattice spacing that can be assigned to the (002) plane of hexagonal WS_2, while the $ZnIn_2S_4$ nanosheet in the composite (Fig. 5(d)) reveals the 0.32 nm lattice fringe which corresponds to the (102) plane of hexagonal $ZnIn_2S_4$. The EDX spectrum of the $ZnIn_2S_4/WS_2$-40%wt composite (Fig. 5e) reveals the characteristic peaks of Zn, In, S and W elements, which evidently indicates the presence of both $ZnIn_2S_4$ and WS_2 in the composite. Notably, the signals of Au and O elements come from the coated gold and environment, respectively. The corresponding EDX elemental mapping (Fig. 5e) shows that the Zn, In, S and W elements are uniformly distributed throughout the composite material. These results clearly show that the $ZnIn_2S_4/WS_2$ heterostructure with intimate and efficient interfacial contact was successfully formed after the microwave heat treatment.

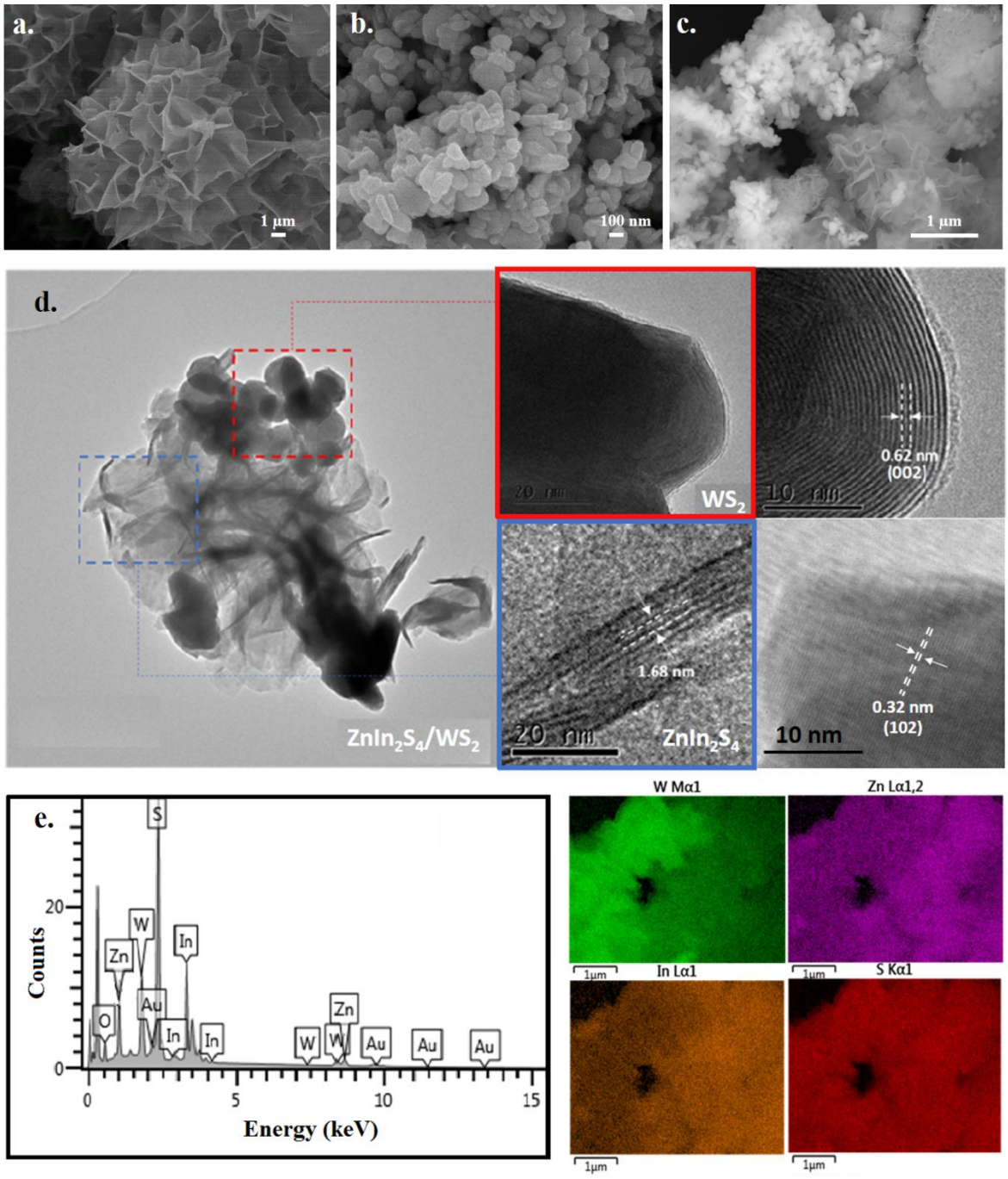

Fig. 5. a.)-c.) SEM images of the $ZnIn_2S_4$, WS_2, and $ZnIn_2S_4/WS_2$-40%wt powders, **b.)** TEM and HRTEM images of the $ZnIn_2S_4/WS_2$-40%wt composite and **d.)** (left) Corresponding EDX spectrum and (right) EDX mapping images of the $ZnIn_2S_4/WS_2$-40%wt composite.

The electrochemical impedance spectroscopy (EIS) Nyquist plot of the $ZnIn_2S_4/WS_2$ heterostructures were studied in comparison to pure $ZnIn_2S_4$ in order to investigate the charge

transfer resistance and the separation efficiency of photo-generated electron-hole pairs. Generally, a diameter of an EIS Nyquist plot is directly proportional to the resistance to the flow of electrons at an interface of an electrode.[43] Thus, larger the Nyquist diameter, higher the charge transfer resistance. As presented in Fig. 6a, the Nyquist diameter of all $ZnIn_2S_4/WS_2$ electrodes are smaller than that of the $ZnIn_2S_4$ electrode. The $ZnIn_2S_4/WS_2$-40%wt electrode provides the smallest Nyquist diameter, indicating the lowest charge transfer resistance. In addition, a larger diameter of the Nyquist plot for the physical mixture of $ZnIn_2S_4$ and WS_2, implies a higher charge transfer resistance in comparison to the $ZnIn_2S_4/WS_2$-40%wt composite, suggesting a poor charge separation efficiency due to the physical interaction between the individual materials.

The photoluminescence (PL) emission spectra of the composites were also studied to investigate the recombination rate of photo-generated electrons and holes. Typically, in a PL experiment, electrons from valence band are excited to conduction band (or sub-bands) at certain excitation wavelength. These electrons may return to the valence band arising a PL signal. The higher PL emission intensity, the higher in the probability of the photo-generated charge carriers being recombined, thus resulting in a lower photocatalytic performance.[53] As shown in Fig. 6b, the PL emission peaks of all samples are centered at 670 nm, and the emission intensities of all $ZnIn_2S_4/WS_2$ composites are lower than that of $ZnIn_2S_4$. These finding clearly indicate that the formation of the $ZnIn_2S_4/WS_2$ heterostructure with intimate and efficient interfacial contact is beneficial to promote photo-generated charge transfer across the heterojunction boundary as well as suppress the photo-generated electron-hole pair recombination, which are consistent with the result from the EIS measurement. Consistently, the $ZnIn_2S_4/WS_2$-40%wt composite shows the weakest PL emission intensity and smallest diameter on EIS Nyquist plot, indicating the most efficient suppression of the charge

recombination as well as the great separation of photo-generated charge carriers and interfacial charge transportation under visible light irradiation. [19 29]

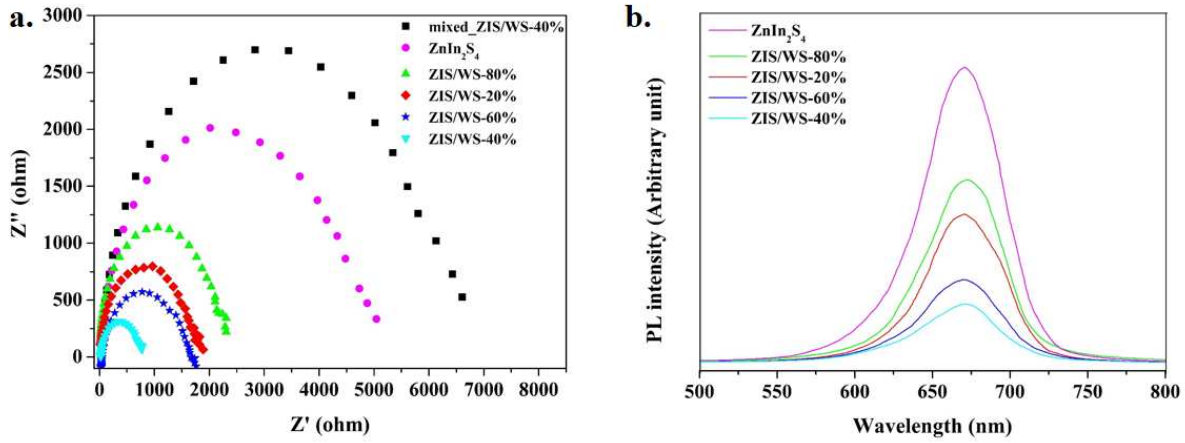

Fig.6. a.) EIS Nyquist plots and **b.)** PL emission spectra of the $ZnIn_2S_4/WS_2$ composites in comparison with $ZnIn_2S_4$.

The band positions of the $ZnIn_2S_4$ and WS_2 photocatalysts were calculated by the following equations; $E_{VB} = E_{CB} + E_g$ and $E_{CB} = X - E_e - 0.5E_g$, derived via the Mulliken electronegativity theory, where E_{VB} is the valence band potential, E_{CB} is the conduction band potential, X is the absolute electronegativity of the semiconductor materials (4.82 eV for $ZnIn_2S_4$[54] and 5.33 eV for WS_2[55]), E_e is the free electrons estimated energy on the hydrogen scale (4.50 eV [53]), and E_g is the $ZnIn_2S_4$ and WS_2 band gap energies. According to the E_g values (2.81 eV for $ZnIn_2S_4$ and 1.83 eV for WS_2) calculated from the UV-visible DRS analysis (Fig. 3a), the V_B and C_B of $ZnIn_2S_4$ are 1.70 eV and -1.11 eV, respectively, and the V_B and C_B of WS_2 are 1.74 eV and -0.09 eV, respectively.

To confirm the E_{VB} and E_{CB} of $ZnIn_2S_4$ and WS_2, Mott-Schottky measurement was carried out. As presented in Fig. 7, the slope of the Mott-Schottky plots of $ZnIn_2S_4$ and WS_2 electrodes are positive, indicating an n-type characteristic of both $ZnIn_2S_4$ and WS_2. In addition, by extrapolating the Mott-Schottky curves to the $1/C^2 = 0$, the flat band potentials

(E_F) of $ZnIn_2S_4$ and WS_2 are -1.22 V and -0.20 V (*vs.* Ag/AgCl), respectively, which correspond to -1.01 V and 0.01 V (*vs.* NHE), respectively. Typically, E_{CB} of an n-type semiconductor is ~0.1 V more negative than its flat band potential.[56] Therefore, the C_B of $ZnIn_2S_4$ and WS_2 is -1.11 eV and -0.09 eV, respectively. Combining with the above E_g values, the E_{VB} of $ZnIn_2S_4$ and WS_2 are 1.70 eV and 1.74 eV, respectively. As summarized in Table 2, the E_{VB} and E_{CB} of $ZnIn_2S_4$ and WS_2 are in accordance with the Mulliken electronegativity data.

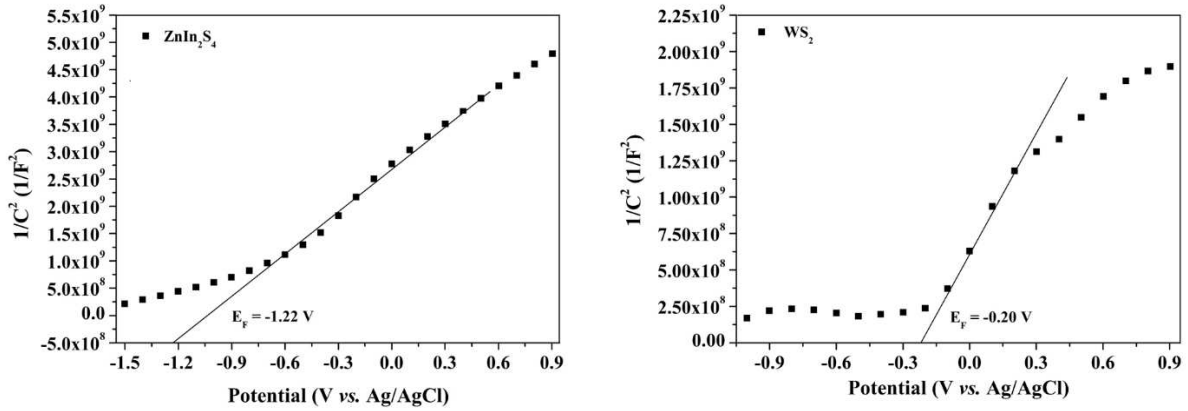

Fig. 7. Mott-Schottky plots of the $ZnIn_2S_4$ and WS_2 electrodes.

Table 2. The E_{VB} and E_{CB} of $ZnIn_2S_4$ and WS_2 calculated according to the Mulliken electronegativity theory and Mott-Schottky measurement.

Electrode	E_g (eV)	Mulliken EN theory			Mott-Schottky plots		
		X (eV)	E_{VB} eV)	E_{CB} (eV)	E_F (eV)	E_{VB} (eV)	E_{CB} (eV)
$ZnIn_2S_4$	2.81	4.82	1.70	-1.11	1.22	1.70	-1.11
WS_2	1.83	5.33	1.74	-0.09	0.20	1.74	-0.09

3.3. Photocatalytic activity of the $ZnIn_2S_4/WS_2$ composite for H_2 production

The photocatalytic H_2 production activities of the $ZnIn_2S_4/WS_2$ photocatalyst samples, evaluated under UV-visible irradiation, in comparison with the $ZnIn_2S_4$ and WS_2 photocatalysts are shown in Fig. 8a. Under the same experimental conditions, all $ZnIn_2S_4/WS_2$ photocatalysts

exhibit higher photocatalytic H_2 production rate than those of either $ZnIn_2S_4$ (145.3 μmol h^{-1} g^{-1}) and WS_2 (44.0 μmol h^{-1} g^{-1}) photocatalysts. With increased the WS_2 loading, the photocatalytic H_2 production activity increases and reaches a maximum at 293.3 μmol h^{-1} g^{-1} when 40%wt of WS_2 is introduced. The improvement of the H_2 production rate is two-times higher than that of the $ZnIn_2S_4$ photocatalyst. In addition, the apparent quantum yield (AQY) of the $ZnIn_2S_4/WS_2$-40%wt photocatalyst reaches 9.22%, which is much higher than that of pure $ZnIn_2S_4$ (3.73%). Moreover, the calculated AQY for the $ZnIn_2S_4/WS_2$-40%wt photocatalyst exhibits much higher quantum yield for H_2 production than the previously reported literatures related to $ZnIn_2S_4$-based composite photocatalysts as summarized in Table S1 (see Supporting Information). These results demonstrate that WS_2 is an effective co-catalyst for improving the photocatalytic efficiency of the $ZnIn_2S_4$ photocatalyst. When the WS_2 content is above 40%wt, the photocatalytic activity is found gradually decrease. This may be because the excess WS_2 on the surface of $ZnIn_2S_4$ not only shields the active site of the $ZnIn_2S_4$ photocatalyst but also blocks the incident light absorption of the composite photocatalyst.[57] From this result, finding the optimum ratios of $ZnIn_2S_4$ and WS_2 in the composite would promote a great separation of photo-generated charge carriers, resulting in an improvement in the photocatalytic activity. The H_2 production activity of the physical mixture of $ZnIn_2S_4$ and 40%wt of WS_2 was also investigated for comparison. As presented in Figure 8a, the $ZnIn_2S_4/WS_2$-40%wt heterojunction photocatalyst exhibits obviously higher H_2 production rate (293.3 μmol h^{-1} g^{-1}) than those of pure $ZnIn_2S_4$ (145.3 μmol h^{-1} g^{-1}) and physical mixture of $ZnIn_2S_4$ and WS_2 (101.3 μmol h^{-1} g^{-1}), indicating that the enhanced photocatalytic activity of the composite is originated by the efficient charges separation and transportation at the chemically contact interface between $ZnIn_2S_4$ and WS_2, corresponding to the EIS and PL studies.

On a basis of the characterization results, a "type-II band alignment" of the $ZnIn_2S_4/WS_2$ heterojunction and a photo-generated charge transfer process are proposed in Fig. 8b. Under UV-visible light irradiation, the $ZnIn_2S_4/WS_2$ photocatalyst is simultaneously excited, generating electron-hole pairs. The photo-generated electrons transfer from the C_B of $ZnIn_2S_4$ to the C_B of WS_2 due to the more positive C_B potential of WS_2 (-0.09 eV) compared to that of $ZnIn_2S_4$ (-1.11 eV). The photo-generated holes can migrate the opposite way through the heterojunction. Then, the accumulated electrons in the C_B of WS_2 reduce H^+ ions to produce H_2 gas since the C_B of WS_2 is more negative than the hydrogen reduction potential (H^+/H_2 = 0.00 V *vs.* NHE).[28] Moreover, the H^+ ions in the solution can strongly bond to the sulfur atoms on exposed WS_2 edges, which is easily reduced to H_2 gas by electrons.[58] At the same time, photo-generated holes react with the sacrificial reagents (S^{2-} and SO_3^{2-}) for oxidation processes.

To evaluate recyclability of the $ZnIn_2S_4/WS_2$-40%wt photocatalyst for the photocatalytic H_2 production, three sequential tests were carried out. As illustrated in Fig. 8c, the H_2 production rate slightly decreases by about 5.7% after three-cycle tests, suggesting that the photocatalyst substantially retains its photocatalytic activity for H_2 production. Furthermore, the photocatalytic H_2 production activities of the $ZnIn_2S_4/WS_2$ composite photocatalyst under UV-visible irradiation (λ > 385 nm) and visible light irradiation (λ > 400 nm) were also investigated in comparison to the $ZnIn_2S_4$ as shown in Fig. 8d. As expected, either $ZnIn_2S_4$ or $ZnIn_2S_4/WS_2$-40%wt photocatalysts appear to be more active in UV-visible region than visible region. In this work, under the UV-visible and visible regions, the H_2 production rate over the $ZnIn_2S_4/WS_2$-40%wt photocatalyst is twice as high in comparison to the pure $ZnIn_2S_4$. This confirms that the $ZnIn_2S_4/WS_2$ composite actives in both UV and visible regions.

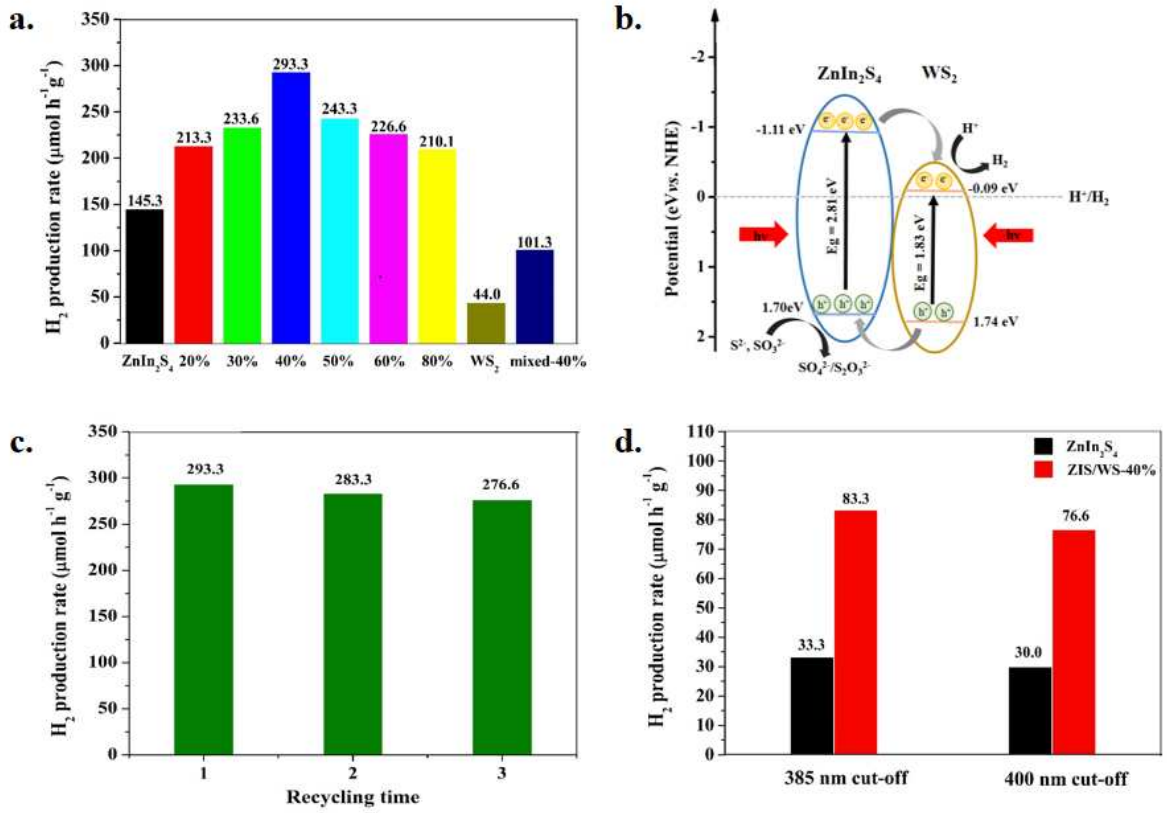

Fig. 8. a.) H_2 production rate of the $ZnIn_2S_4$, WS_2 and $ZnIn_2S_4/WS_2$ photocatalysts under UV-visible light irradiation, **b.)** a "type-II band alignment" and a photo-generated charge transfer in the $ZnIn_2S_4/WS_2$ heterojunction, **c.)** recyclability of the $ZnIn_2S_4/WS_2$-40%wt photocatalyst under UV-visible light irradiation during 3 h, and **d.)** H_2 production rate of the $ZnIn_2S_4/WS_2$-40%wt photocatalyst under UV-visible and visible regions using 385 nm and 400 nm filter cut-off, respectively, in comparison with the $ZnIn_2S_4$ photocatalyst.

3.4. Photocatalytic activity of the $ZnIn_2S_4/WS_2$ composite for Cr(VI) reduction

The photocatalytic Cr(VI) reduction activities of the $ZnIn_2S_4$, WS_2 and $ZnIn_2S_4/WS_2$-40%wt are illustrated in Fig. 9a. The blank experiment without the $ZnIn_2S_4$, WS_2 and $ZnIn_2S_4/WS_2$-40%wt photocatalysts shows no apparent photocatalytic activity, suggesting that Cr(VI) is highly stable during photolytic reaction. After stirring in the dark condition for 30 min, pure $ZnIn_2S_4$ shows higher adsorption capacity than $ZnIn_2S_4/WS_2$-40%wt and pure WS,

respectively, corresponding to the BET surface area analysis (46, 39 and 15 m^2/g for pure $ZnIn_2S_4$, $ZnIn_2S_4/WS_2$-40%wt and pure WS_2, respectively). The $ZnIn_2S_4/WS_2$-40%wt composite exhibits higher photoreduction efficiency than those single materials under the same irradiation times. The photoreduction efficiency of the $ZnIn_2S_4/WS_2$-40%wt, $ZnIn_2S_4$ and WS_2 are 93.6%, 78.4% and 4.2%, respectively, after 120 min of the light irradiation. The reaction kinetics is consistent with a pseudo-first-order model, which is suitable for a low concentration of solution, and obtained by the following equation; $\ln(C_0\text{-}C) = kt$, where k is the Cr(VI) reduction rate constant and t is the irradiation time. As shown in Fig. 9b, the determined rate constant (k) of the $ZnIn_2S_4/WS_2$-40%wt, $ZnIn_2S_4$ and WS_2 are $2.1\text{x}10^{-2}$, $1.0\text{x}10^{-2}$ and $0.02\text{x}10^{-3}$ min^{-1}, respectively, with good linear correlation coefficients ($R^2 > 0.97$). The rate constant for the Cr(VI) reduction of the $ZnIn_2S_4/WS_2$-40%wt exhibits two times higher than that of the $ZnIn_2S_4$, corresponding with the photocatalytic H_2 production results. Even though the BET surface area of the $ZnIn_2S_4/WS_2$-40%wt composite slightly decreases when compared to pure $ZnIn_2S_4$, the composite exhibits the highest photocatalytic efficiency. This demonstrates that, in this case, surface area does not significantly affect the photocatalytic activity of the $ZnIn_2S_4/WS_2$ photocatalyst.

In addition, the Cr(VI) photoreduction of the physical mixture of $ZnIn_2S_4$ and WS_2 was tested. As shown in Fig. 9a and 9b, the $ZnIn_2S_4/WS_2$-40%wt composite photocatalyst exhibits enhanced efficiency in comparison to the physical mixture (44.4% with the k value of $0.4\text{x}10^{-2}$ min^{-1}). In addition, the apparent quantum yield (AQY) of the $ZnIn_2S_4/WS_2$-40%wt composite was calculated to be 5.89% which is about 1.2 times higher than that of $ZnIn_2S_4$ (4.72%) and was close to the previously reported literature related to $ZnIn_2S_4$-based composite photocatalyst as presented in Table S2 (see Supporting Information). These results illustrated that the combination between $ZnIn_2S_4$ and WS_2 is a promising approach to improve the photocatalytic activity of $ZnIn_2S_4$.

The effect of pH value of the Cr(VI) solution on the photoreduction efficiency of the $ZnIn_2S_4/WS_2$-40%wt photocatalyst was also investigated by varying the pH value in range of 4 to 8 with the constant photocatalyst dosage and initial Cr(VI) concentration (Fig. 9c). When the pH value is decreased from 6 (initial pH) to 4, the photoreduction activity is increased from 93.6 to 98.5% with the *k* value of $3.3x10^{-2}$ min^{-1} (Fig. 9d). However, in the basic solution (pH = 8), the photoreduction efficiency is decreased to 9.3% with the *k* value of $1.1x10^{-3}$ min^{-1}. This is probably because, during the Cr(VI) reduction, $Cr(OH)_3$ produced from CrO_4^{2-} ion (Equation (6)) coats on the active surface of the photocatalyst, lowering the Cr(VI) reduction activity.[59] [60] In addition, CrO_4^{2-} in the basic solution is not easier to be reduced than $Cr_2O_7^{2-}$ and $HCrO_4^-$ in acidic solution due to a lower reduction potential of CrO_4^{2-}/Cr^{3+} (-0.13 V *vs.* NHE) than that of $Cr_2O_7^{2-}/Cr^{3+}$ (1.23 V *vs.* NHE) and $HCrO_4^-/Cr^{3+}$ (1.35 V *vs.* NHE).[4] Furthermore, according to the Le Chatelier's principle[61], the increase in the concentration of hydroxide (OH^-) ions or decrease in the concentration of protons (H^+) results in a slower reach of the chemical equilibrium (Equation (6)), suggesting that Cr(VI) ion is effectively reduced to Cr(III) ion in the acidic solution rather than the basic solution.

UV-vis absorption spectral change of the Cr(VI) solution during the photoreduction reaction in the presence of the $ZnIn_2S_4/WS_2$-40%wt photocatalyst at pH = 4 (Fig. 9e) illustrate that the absorption peak intensity of Cr(VI) at 532 nm gradually decrease with increasing irradiation time and the Cr(VI) photoreduction is almost completed when the irradiation is continued up to 120 min. To confirm an occurrence of Cr(III) ions after photocatalysis, the NaOH solution was added into the Cr(VI) solutions before and after 120 min of light irradiation. A pale gray precipitate of $Cr(OH)_3$ immediately took place for the solution after the light irradiation.[62] These results evidently indicate that Cr(VI) ion has been completely reduced to Cr(III) ion.

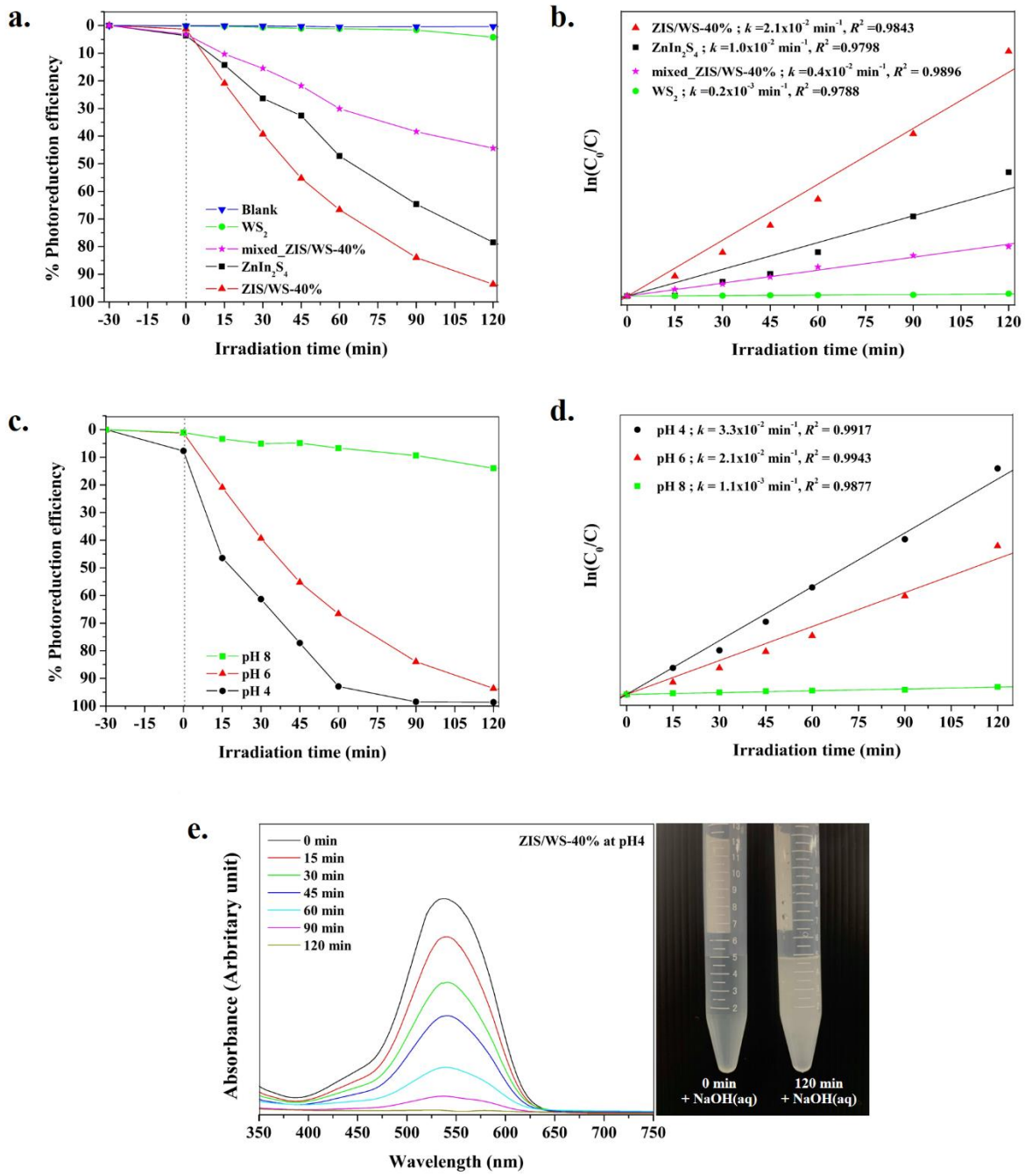

Fig. 9. a.) Photoreduction efficiency and **b.)** pseudo-first-order kinetics of the Cr(VI) photoreduction at pH 6 (the initial pH of the solution). **c.)** Effect of pH of the solution and **d.)** pseudo-first-order kinetics of the Cr (VI) photoreduction. **e.)** (left) UV-vis absorption spectra change of the Cr(VI) solution during the photoreduction reaction in the presence of the $ZnIn_2S_4/WS_2$-40%wt photocatalyst at pH = 4 and (right) the change that took place when

NaOH solution was added to the Cr(VI) solutions before and after visible light irradiation for 120 min.

The recyclability of the $ZnIn_2S_4/WS_2$-40%wt photocatalyst for the photoreduction of Cr(VI) reaction was investigated by a three-run cycle test at pH of the solution of 4. The result (Fig. 10a) shows an insignificantly decreased efficiency by about 5.4% after three cycles. This result indicates that the $ZnIn_2S_4/WS_2$-40%wt photocatalyst provides a good recyclability for the Cr(VI) photoreduction. Notably that the slightly decreased efficiencies for the Cr(VI) photoreduction and H_2 production are probably because the loss of the photocatalyst during the recovery process. XRD spectra and SEM images of the $ZnIn_2S_4/WS_2$-40%wt photocatalyst after three-cycle test were analyzed to evaluate its photostability for the photocatalytic H_2 production and Cr(VI) photoreduction. The XRD spectra (Fig. 10b) of the fresh photocatalyst, and the used photocatalyst reveal that the diffraction reflections are little (not significant) changed after the photocatalytic recycling. In addition, the FESEM images show that the morphologies of $ZnIn_2S_4$ and WS_2 in the $ZnIn_2S_4/WS_2$-40%wt composite photocatalyst remain unchanged (Fig. 10c-10d). These results imply that the $ZnIn_2S_4/WS_2$-40%wt photocatalyst is reusable and stable under the reaction conditions.

A possible mechanism for the photocatalytic Cr(VI) reduction process is illustrated in Fig. 10e. Since the C_B of WS_2 (-0.09 eV) is more negative than the reduction potential of Cr(VI)/Cr(III) (1.33 V *vs.* NHE)[63], the photo-generated electrons can reduce the Cr(VI) ion to Cr(III) ion. Simultaneously, the H_2O can be oxidized to O_2 by the photo-generated holes since the reduction potential of O_2/H_2O (1.23 V *vs.* NHE) is less positive than the V_B of $ZnIn_2S_4$ (1.70 eV).[64] The reaction steps are also provided as follows [4] ;

$$ZnIn_2S_4/WS_2 + h\nu\ (\text{visible}) \rightarrow ZnIn_2S_4\,(e_{CB}^- + h_{VB}^+) + WS_2\,(e_{CB}^- + h_{VB}^+) \quad (1)$$

$$ZnIn_2S_4\,(e_{CB}^- + h_{VB}^+) + WS_2\,(e_{CB}^- + h_{VB}^+) \rightarrow ZnIn_2S_4\,(h_{VB}^+) + WS_2\,(e_{CB}^-) \quad (2)$$

$$2H_2O + ZnIn_2S_4\,(4h_{VB}^{+}) \rightarrow O_2 + 4H^{+} \quad (3)$$

under acidic condition,

$$Cr_2O_7^{2-} + 14H^{+} + WS_2\,(6e_{CB}^{-}) \rightarrow 2Cr^{3+} + 7H_2O \quad (4)$$

$$HCrO_4^{-} + 7H^{+} + WS_2\,(3e_{CB}^{-}) \rightarrow Cr^{3+} + 4H_2O \quad (5)$$

under basic condition,

$$CrO_4^{2-} + 4H_2O + WS_2\,(3e_{CB}^{-}) \rightarrow Cr(OH)_3 + 5OH^{-} \quad (6)$$

Based on the photocatalytic experimental results, WS_2 acts as an efficient co-catalyst in the $ZnIn_2S_4/WS_2$ system. More importantly, the intimate interface between $ZnIn_2S_4$ and WS_2 facilitates the photo-generated charge carriers transfer between $ZnIn_2S_4$ and WS_2 through heterojunction between the surface interaction, which is an vital factor for improving the photocatalytic activity of the $ZnIn_2S_4/WS_2$ composite for the Cr(VI) reduction and H_2 production.

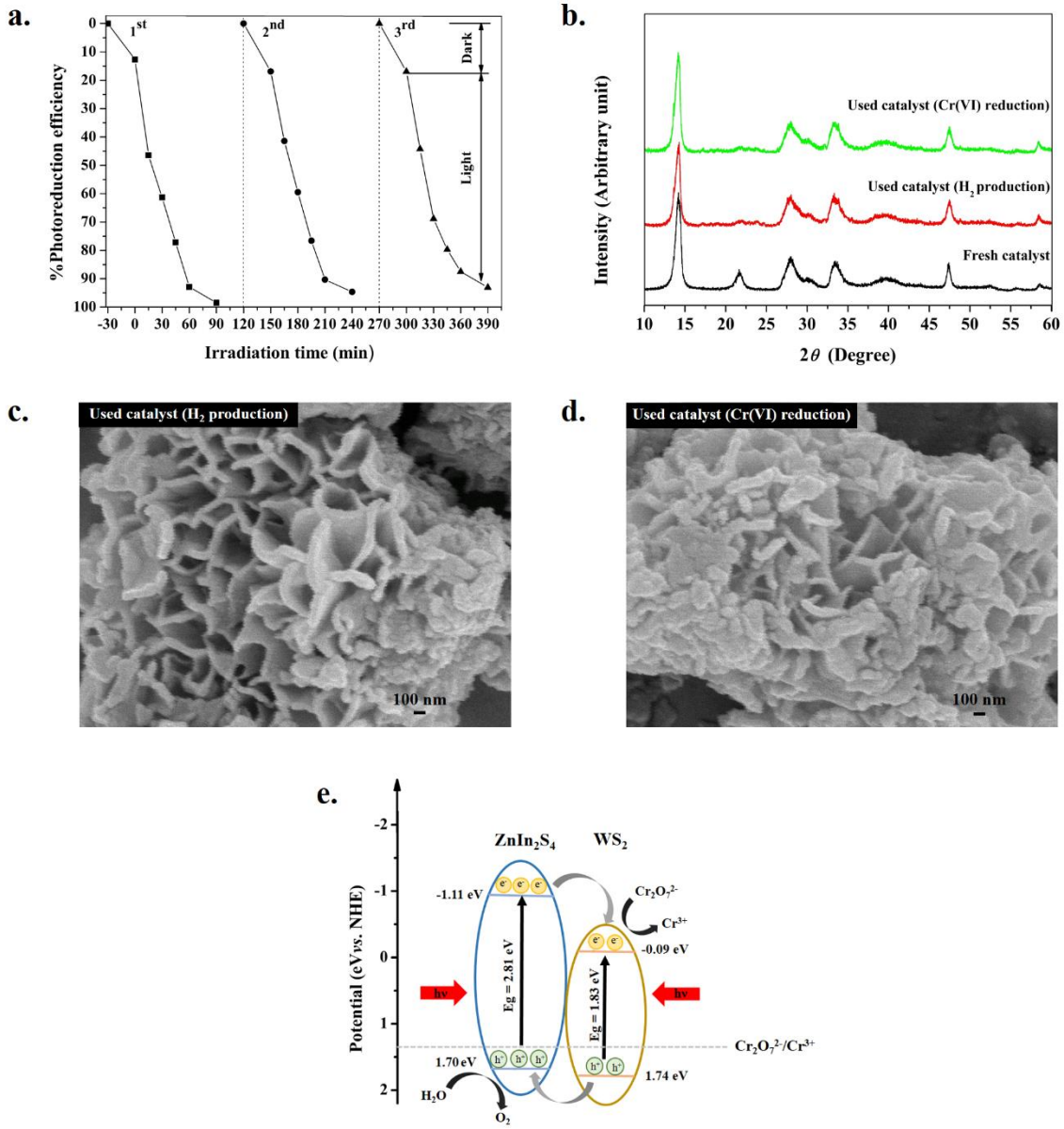

Fig. 10. a.) Recyclability of the $ZnIn_2S_4/WS_2$-40%wt photocatalyst performed at pH 4. **b.)** XRD patterns and **c.)-d.)** FESEM images of the used $ZnIn_2S_4/WS_2$-40%wt photocatalysts after three-cycle test. **e.)** a proposed mechanism of the Cr(VI) photoreduction by the $ZnIn_2S_4/WS_2$-40%wt photocatalyst under visible light irradiation.

Conclusions

$ZnIn_2S_4/WS_2$ composites with well-defined flower-like $ZnIn_2S_4$ microspheres were successfully synthesized by microwave synthesis method using L-cysteine as the sulfur source

and applied for photocatalytic H_2 production and Cr(VI) photoreduction. The loading amount of WS_2 played an important role on the photocatalytic H_2 production activity under UV-visible light irradiation. The $ZnIn_2S_4/WS_2$-40%wt photocatalyst exhibited the highest H_2 production rate. In addition, this composite photocatalyst also exhibited excellent photocatalytic Cr(VI) reduction activity under visible light irradiation where the photoreduction efficiency of the composite photocatalyst was better for the acidic solutions (pH 4 and 6) than that for the basic solution (pH 8). Moreover, the $ZnIn_2S_4/WS_2$ photocatalyst show excellent recyclability with minimal loss of the photoactivity on use and good stability during the photocatalytic processes. The enhanced photocatalytic performance of the $ZnIn_2S_4/WS_2$ photocatalyst was ascribed to the efficient separation and transportation of the photo-generated electron–hole pairs through the "type II heterojunction" at the interface in the $ZnIn_2S_4/WS_2$ composite as well as the increase in the visible-light response. The results of this work demonstrated that the synthesized $ZnIn_2S_4/WS_2$ composite is a promising photocatalyst for the applications in photocatalytic H_2 production and heavy metal ion pollutants elimination. Besides that, the microwave synthesis method is the potentially useful method for preparing of either the single-component $ZnIn_2S_4$ or the $ZnIn_2S_4/WS_2$ composite material as well as other composite materials.

Acknowledgments

This research work was partially supported by Chiang Mai University, the Center of Excellence for Innovation in Chemistry (PERCH-CIC), Ministry of Higher Education, Science, Research and Innovation, and the Center of Excellence (CoE) in Materials Science and Technology. The authors would like to acknowledge the Science Achievement Scholarship of Thailand, and the Graduate School, Chiang Mai University, Thailand for financial support towards Watcharapong Pudkon.

References

1. K. Zhang and L. Guo, *Catal. Sci. Tech.*, 2013, **3**, 1672-1690.
2. C. E. Barrera-Díaz, V. Lugo-Lugo and B. Bilyeu, *J. Hazard. Mater.*, 2012, **223-224**, 1-12.
3. J. Hu, Y. Ji, Z. Mo, N. Li, Q. Xu, Y. Li, H. Xu, D. Chen and J. Lu, *J. Mater. Chem. A*, 2019, **7**, 4408-4414.
4. G. Zhang, D. Chen, N. Li, Q. Xu, H. Li, J. He and J. Lu, *Appl. Catal. B: Environ.*, 2019, **250**, 313-324.
5. A. B. Djurišić, Y. H. Leung and A. M. Ching Ng, *Mater. Hori.*, 2014, **1**, 400-410.
6. M. A. Malati and W. K. Wong, *Surf. Techol.*, 1984, **22**, 305-322.
7. J. Hu, D. Chen, Z. Mo, N. Li, Q. Xu, H. Li, J. He, H. Xu and J. Lu, *Angew. Chem. Int. Ed.*, 2019, **131**, 2095-2099.
8. J. Xu and X. Cao, *Chem. Eng. J.*, 2015, **260**, 642-648.
9. N. Romeo, A. Dallaturca, R. Braglia and G. Sberveglieri, *Appl. Phys. Lett.*, 1973, **22**, 21-22.
10. W. S. Seo, R. Otsuka, H. Okuno, M. Ohta and K. Koumoto, *J. Mater. Res.*, 2011, **14**, 4176-4181.
11. S. Peng, M. Dan, F. Guo, H. Wang and Y. Li, *Colloids Surf. A: Physicochem. Eng. Asp.*, 2016, **504**, 18-25.
12. L. Mandal, N. S. Chaudhari and S. Ogale, *ACS Appl. Mater. Interfaces*, 2013, **5**, 9141-9147.
13. S. Shen, L. Zhao and L. Guo, *Int. J. Hydrog. Energy*, 2008, **33**, 4501-4510.
14. B. Liu, X. Liu, L. Li, J. Li, C. Li, Y. Gong, L. Niu, X. Zhao and C. Q. Sun, *Chinese J. Catal.*, 2018, **39**, 1901-1909.

15. S. Zhang, X. Liu, C. Liu, S. Luo, L. Wang, T. Cai, Y. Zeng, J. Yuan, W. Dong, Y. Pei and Y. Liu, *ACS Nano*, 2018, **12**, 751-758.

16. R. Marschall, *Adv. Funct. Mater.*, 2014, **24**, 2421-2440.

17. L. Su, X. Ye, S. Meng, X. Fu and S. Chen, *Appl. Surf. Sci.*, 2016, **384**, 161-174.

18. K. Song, R. Zhu, F. Tian, G. Cao and F. Ouyang, *J. Solid State Chem.*, 2015, **232**, 138-143.

19. T. Huang, W. Chen, T. Y. Liu, Q. L. Hao and X. H. Liu, *Powder Technol.*, 2017, **315**, 157-162.

20. B. Gao, L. Liu, J. Liu and F. Yang, *Appl.Catal. B: Environ.*, 2013, **129**, 89-97.

21. B. Fan, Z. Chen, Q. Liu, Z. Zhang and X. Fang, *Appl. Surf. Sci.*, 2016, **370**, 252-259.

22. S. Shen, J. Chen, X. Wang, L. Zhao and L. Guo, *J. Power Sources*, 2011, **196**, 10112-10119.

23. T. Liu, W. Chen, T. Huang, G. Duan, X. Yang and X. Liu, *J. Mater. Sci.*, 2016, **51**, 6987-6997.

24. G. Zhang, D. Chen, N. Li, Q. Xu, H. Li, J. He and J. Lu, *Appl. Catal. B: Environ.*, 2018, **232**, 164-174.

25. Z. Mei, S. Ouyang, D.-M. Tang, T. Kako, D. Golberg and J. Ye, *Dalton Trans.*, 2013, **42**, 2687-2690.

26. W. Cui, D. Guo, L. Liu, J. Hu, D. Rana and Y. Liang, *Catal. Commun.*, 2014, **48**, 55-59.

27. Y. Yu, G. Chen, G. Wang and Z. Lv, *Int. J. Hydrog. Energy*, 2013, **38**, 1278-1285.

28. L. Wei, Y. Chen, Y. Lin, H. Wu, R. Yuan and Z. Li, *Appl. Catal. B: Environ.*, 2014, **144**, 521-527.

29. D. Zeng, L. Xiao, W.-J. Ong, P. Wu, H. Zheng, Y. Chen and D.-L. Peng, *Chem. Sus. Chem.*, 2017, **10**, 4624-4631.

30. X. Zong, J. Han, G. Ma, H. Yan, G. Wu and C. Li, *J. Phys. Chem.C*, 2011, **115**, 12202-12208.

31. X. Li, M. Su, G. Zhu, K. Zhang, X. Zhang and J. Fan, *Dalton Trans.*, 2018, **47**, 10046-10056.

32. H. Lu, J. Wang, H. Hao and T. Wang, *Nanomaterials (Basel)*, 2017, **7**, 303(2)-303(19).

33. S. V. P. Vattikuti, C. Byon and C. V. Reddy, *Mater. Res. Bull.*, 2016, **75**, 193-203.

34. K. M. McCreary, A. T. Hanbicki, G. G. Jernigan, J. C. Culbertson and B. T. Jonker, *Sci. Rep.*, 2016, **6**, 19159(1)-19159(7).

35. C. Feng, L. Huang, Z. Guo and H. Liu, *Electrochem. Commun.*, 2007, **9**, 119-122.

36. D. Genuit, P. Afanasiev and M. Vrinat, *J. Catal.*, 2005, **235**, 302-317.

37. T. Chiranjeevi, P. Kumar, S. K. Maity, M. S. Rana, G. Murali Dhar and T. S. R. Prasada Rao, *Microporous Mesoporous Mater.*, 2001, **44-45**, 547-556.

38. I. B. Assaker, M. Gannouni, J. B. Naceur, M. A. Almessiere, A. L. Al-Otaibi, T. Ghrib, S. Shen and R. Chtourou, *Appl. Surf. Sci.*, 2015, **351**, 927-934.

39. J. Gao, C. Liu, F. Wang, L. Jia, K. Duan and T. Liu, *Nanoscale Res. Lett.*, 2017, **12**, 377(1)-377(9).

40. J. Zhou, D. Chen, L. Bai, L. Qin, X. Sun and Y. Huang, *Int. J. Hydrog. Energy*, 2018, **43**, 18261-18269.

41. N. Chumha, T. Thongtem, S. Thongtem, D. Tantraviwat, S. Kittiwachana and S. Kaowphong, *Ceram. Int.*, 2016, **42**, 15643-15649.

42. A. B. Yousaf, M. Imran, S. J. Zaidi and P. Kasak, *Sci. Rep.*, 2017, **7**, 6574(1)-6574(10).

43. S. Xu, J. Dai, J. Yang, J. You and J. Hao, *Nanomaterials (Basel)*, 2018, **8**, 472(1)-472(17).

44. A. L. Patterson, *Phys. Rev.*, 1939, **56**, 978-982.

45. Y. Chen, S. Hu, W. Liu, X. Chen, L. Wu, X. Wang, P. Liu and Z. Li, *Dalton Trans.*, 2011, **40**, 2607-2613.

46. J. Zhong, Q. Wang and W. Cai, *Mater. Lett.*, 2015, **150**, 69-72.

47. M. Sabet, M. Salavati-Niasari and E. Esmaeili, *J. Inorg. Organomet. Polym. Mater.*, 2016, **26**, 738-743.

48. N. Chumha, T. Thongtem, S. Thongtem, S. Kittiwachana and S. Kaowphong, *Appl. Surf. Sci.*, 2018, **447**, 292-299.

49. X. Hu, J. C. Yu, J. Gong and Q. Li, *Crys. Growth Des.*, 2007, **7**, 2444-2448.

50. Y. Huo, J. Zhang, M. Miao and Y. Jin, *Appl. Catal. B: Environ.*, 2012, **111-112**, 334-341.

51. P. Qiu, J. Yao, H. Chen, F. Jiang and X. Xie, *J. Hazard. Mater.*, 2016, **317**, 158-168.

52. J. Liqiang, Q. Yichun, W. Baiqi, L. Shudan, J. Baojiang, Y. Libin, F. Wei, F. Honggang and S. Jiazhong, *Sol. Energy Mater. Sol. Cells*, 2006, **90**, 1773-1787.

53. Z. Zhang, L. Huang, J. Zhang, F. Wang, Y. Xie, X. Shang, Y. Gu, H. Zhao and X. Wang, *Appl. Catal. B: Environ.*, 2018, **233**, 112-119.

54. Y. J. Yuan, J. R. Tu, Z. J. Ye, D. Q. Chen, B. Hu, Y. W. Huang, T. T. Chen, D. P. Cao, Z. T. Yu and Z. G. Zou, *Appl. Catal. B: Environ.* 2016, **188**, 13-22.

55. E. C. Cho, C. W. Chang-Jian, J. H. Zheng, J. H. Huang, K. C. Lee, B. C. Ho and Y. S. Hsiao, *J. Taiwan Inst. Chem. E.*, 2018, **91**, 489-498.

56. W. Guo, W. D. Chemelewski, O. Mabayoje, P. Xiao, Y. Zhang and C. B. Mullins, *J. Phys. Chem. C*, 2015, **119**, 27220-27227.

57. J. He, L. Chen, Z. Q. Yi, C. T. Au and S. F. Yin, *Ind. Eng. Chem. Res.*, 2016, **55**, 8327-8333.

58. H. G. Füchtbauer, A. K. Tuxen, P. G. Moses, H. Topsøe, F. Besenbacher and J. V. Lauritsen, *Phys.Chem.Chem. Phys.*, 2013, **15**, 15971-15980.

59. M. Shirzad Siboni, M. T. Samadi, J. K. Yang and S. M. Lee, *Environ. Technol.*, 2011, **32**, 1573-1579.

60. M. Shirzad-Siboni, M. Farrokhi, R. Darvishi Cheshmeh Soltani, A. Khataee and S. Tajassosi, *Ind. Eng. Chem. Res.*, 2014, **53**, 1079-1087.

61. M. J. Sienko and R. A. Plane,*Chemical Principles and Properties*, McGraw-Hill, New York, 2nd edn., 1974.

62. M. J. Mohammed and E. N. Lambert, *Comprehensive Qualitative Analysis for Advaced Level Chemistry*, Heinemann, London, 1st edn., 1978.

63. Y. Kim, H. Joo, N. Her, Y. Yoon, C. H. Lee and J. Yoon, *Chem. Eng. J.*, 2013, **229**, 66-71.

64. S. Nezar, Y. Cherifi, A. Barras, A. Addad, E. Dogheche, N. Saoula, N. A. Laoufi, P. Roussel, S. Szunerits and R. Boukherroub, *Arab. J. Chem.*, 2019, **12**, 215-224.